JOURNAL OF SPACECRAFT AND ROCKETS
Vol. 36, No. 2, March–April 1999

# Thermostructural Analysis of X-34 Wing Leading-Edge Tile Thermal Protection System

Frank S. Milos[*] and Thomas H. Squire[†]
*NASA Ames Research Center, Moffett Field, California 94035-1000*

**Finite element thermal and stress analyses are presented for ceramic tiles, assemblies, and arc jet models relevant to the thermal protection system for the X-34 wing leading edge. The analyses are performed to verify thermal and structural models for silicone impregnated reusable ceramic ablator, to establish a failure criterion for stressed tiles, to simulate the response of the wing leading-edge thermal protection system under flight aerothermal and mechanical loads, and to confirm that the design has adequate safety margins. The final design with 0.04-in. intertile gaps is found to meet all thermal and structural requirements.**

## Nomenclature

$C_T$ = heat transfer coefficient, Btu/ft$^2$-s-°F
$c_p$ = specific heat, Btu/lbm-°F
$k$ = thermal conductivity, Btu/h-ft-°F
$q_{\text{cond}}$ = conduction heat flux, Btu/ft$^2$-s
$T$ = temperature, °F
$T_\infty$ = environment temperature for radiation, °F
$\varepsilon$ = emissivity
$\sigma$ = Stephan–Boltzmann constant, Btu/h-ft$^2$-R$^4$

*Subscripts*

$o$ = initial
$R$ = recovery
$w$ = surface

## Introduction

THE X-34 reusable launch vehicle is a winged rocket that deploys from a modified L-1011 aircraft, launches into a suborbital trajectory (up to 260 kft altitude), and returns to Earth for a runway landing. A severe entry produces a peak nosecap hot-wall heat flux of about 15 Btu/ft$^2$-s corresponding to Mach 7.7 velocity at an altitude of 140 kft (Ref. 1). The thermal protection system (TPS) consists primarily of flexible blanket insulation except for the nosecap and leading edges where the shear and heating environment warrant the use of a rigid ceramic tile insulation.

The baseline tile material is fibrous refractory composite insulation (FRCI-12) tile impregnated with silicone. This composite, known as silicone impregnated reusable ceramic ablator (SIRCA),[2] is not used as an ablator in this context but as a reusable material. The silicone impregnation renders the tile water resistant, very impermeable to gas flow,[3] and relatively easy to bond to other materials as well as to repair. At sufficiently high temperatures the silicone partially decomposes and reacts with silica fibers in the tile to form a high emissivity glassy char on heated surfaces.

SIRCA samples were subject to thermal and mechanical testing as part of the material development program and flight qualification as TPS for the Mars Pathfinder vehicle.[2] No surface recession or degradation was observed for hot-wall heat fluxes up to 43 Btu/ft$^2$-s (surface temperature of 2750°F). Because the maximum heating rate on the nosecap and the leading edges of X-34 is significantly below that required for surface recession, the primary issues for use of SIRCA as X-34 TPS are demonstration of reusability and verification of adequate safety margins for the TPS assembly under expected aerothermal and structural loads. This paper documents relevant thermal and structural analyses that were performed at NASA Ames Research Center in fulfillment of this task.[4]

The COSMOS/M finite element (FE) analysis software[5] was used for all work presented herein. Steady and quasistatic, small deformation (linear stress) analyses were performed because COSMOS/M does not support nonlinear analysis with orthotropic material properties. However, this assumption is reasonable for the relatively small deflections considered in this work.

## Thermal and Mechanical Models

Thermal and mechanical properties of virgin and char SIRCA were obtained from analysis of tests performed during the material development research and the flight qualification of SIRCA for the Mars Pathfinder vehicle.[2,6] Arc jet and mechanical tests performed at NASA Ames Research Center as part of the X-34 program have provided additional data for validation of the material and computational models. This section describes the experiments and compares model predictions with the test data.

Tables 1–8 list material properties used in this work. The thermal properties were partially derived from analysis of arc-jet test data.[6] The mechanical properties and coefficient of thermal expansion (CTE) of virgin SIRCA are similar to those of the AETB-12 substrate because the added silicone is nonrigidizing. Char mechanical properties have not been measured but are assumed to be the same as the virgin material. Except for CTE, mechanical properties are approximately constant up to 1600°F. Above this temperature, the strength and modulus are assumed to decrease linearly with temperature. Additional property information is provided in the TPSX code.[7]

Owing to the compression stage of the tile-billet manufacturing process, tile properties are orthotropic. The compression axis is termed the transverse direction, and directions perpendicular to the axis are termed in-plane. The transverse direction has lower thermal conductivity and lower mechanical strength than the in-plane direction. To take advantage of the lower transverse conductivity, tiles typically are machined with the transverse direction oriented perpendicular to the heated surface.

### Arc-Jet Life-Cycle Tests

X-34 tile TPS is required to survive 25 missions with only minor refurbishment. To demonstrate this reusability of SIRCA, a wing leading-edge tile model was tested repeatedly in the 20-MW Aerodynamic Heating Facility arc jet at NASA Ames Research Center. Figure 1 shows a cross section drawing of the tile-model geometry. The tile had 1.5-in. outer radius, 0.5-in. inner radius, and 10-in. span in the direction normal to the drawing. The tile was oriented with the transverse direction parallel to the stagnation line. To minimize

---

Received July 27, 1998; revision received Nov. 25, 1998; accepted for publication Dec. 28, 1998.

[*] Aerospace Engineer, Thermal Protection Materials and Systems Branch. Senior Member AIAA.

[†] Senior Research Scientist, ELORET Thermosciences Institute.

Table 1 SIRCA-15F virgin properties,[a] 16 lbm/ft$^3$

| T, °F | $c_p$, Btu/lbm-R | $k$, Btu/h-ft-R | $\varepsilon$ |
|---|---|---|---|
| 31 | 0.241 | 0.0357 | 0.2 |
| 199 | 0.292 | 0.0380 | 0.2 |
| 751 | 0.327 | 0.0431 | 0.5 |
| 1111 | 0.332 | 0.0577 | 0.8 |
| 1471 | 0.337 | 0.0882 | 0.92 |
| 1831 | 0.341 | 0.1020 | 0.92 |
| 2191 | 0.346 | 0.1130 | 0.92 |
| 2551 | 0.350 | 0.1680 | 0.92 |

[a] Transverse $k$ is tabulated. In-plane $k$ is up to 15% larger.

Table 2 SIRCA-15F char properties,[a] 14 lbm/ft$^3$

| T, °F | $c_p$, Btu/lbm-R | $k$, Btu/h-ft-R | $\varepsilon$ |
|---|---|---|---|
| 40 | 0.160 | 0.0154 | 0.8 |
| 329.5 | 0.223 | 0.0173 | 0.8 |
| 618.9 | 0.263 | 0.0202 | 0.8 |
| 908.4 | 0.283 | 0.0293 | 0.8 |
| 1197.9 | 0.294 | 0.0339 | 0.9 |
| 1487.4 | 0.300 | 0.0384 | 0.9 |
| 1776.8 | 0.303 | 0.0676 | 0.9 |
| 2066.3 | 0.303 | 0.0823 | 0.9 |
| 2355.8 | 0.303 | 0.0856 | 0.9 |
| 2551.8 | 0.303 | 0.0856 | 0.9 |

[a] Transverse $k$ is tabulated. In-plane $k$ is up to 30% larger.

Table 3 SIRCA-15F mechanical properties

| Property | Transverse, psi | In-plane, psi |
|---|---|---|
| Tensile strength | 108 | 289 |
| Tensile modulus | 10,200 | 49,000 |
| Compressive strength | 140 | 280 |

Table 4 SIRCA-15F coefficient of thermal expansion

| $T$, °F | CTE, °F$^{-1}$ |
|---|---|
| −16.9 | 7.2E-07 |
| 256.4 | 9.2E-07 |

Table 5 SIP thermal properties, 5.4 lbm/ft$^3$

| $T$, °F | $c_p$, Btu/lbm-R | $k$, Btu/h-ft-R |
|---|---|---|
| −250 | 0.241 | 0.300 |
| 0 | 0.292 | 0.312 |
| 100 | 0.327 | —— |
| 200 | 0.332 | 0.320 |
| 300 | 0.337 | —— |
| 400 | 0.341 | 0.335 |
| 600 | 0.346 | 0.345 |
| 800 | 0.350 | —— |

Table 6 Gr/Ep thermal properties, 112 lbm/ft$^3$

| $c_p$, Btu/lbm-R | $k$, Btu/h-ft-R |
|---|---|
| 0.21 | 10.0 |

Table 7 SIP and Gr/Ep mechanical properties

| Material | Tensile modulus, psi | Tensile strength, psi |
|---|---|---|
| Gr/Ep | 8,000 | 110,000 |
| SIP | 35 | 65 |

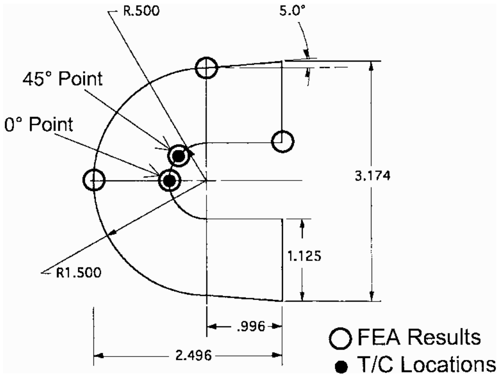

Fig. 1 Cross section of wing leading-edge arc-jet model.

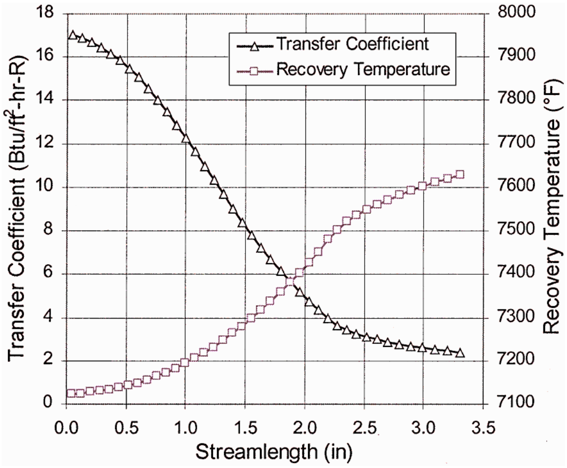

Fig. 2 Arc-jet convective boundary conditions.

incidental heating of the inner surface, the ends of the model were closed, and the interior gap was filled with SilFrax silica foam insulation. Thermocouples were located midspan at the interior points labeled 0 and 45 deg on the figure. Also shown are the locations of five reference points where FE results will be plotted.

The model was centered in the arc-jet flowfield at zero angle of attack and zero yaw, thus the midspan plane was a plane of symmetry. The nominal heating conditions provided a peak surface temperature of about 2250°F, which is higher than expected in flight, and the exposure time of 180 s provided a heat load at least 30% greater than expected at the highest heating location on the wing leading edge. The model was cycled 15 times, then cored at several locations to determine char depth and properties. Virgin SIRCA plugs were bonded into the core holes, and the model was tested another 12 times. Tile damage was limited to very shallow surface cracks in the char layer. A gradual decrease in surface emissivity was observed, but this trend was mitigated by a single application of a SIRCA-compatible emissivity coating after cycle 10. (The composition and procedure cannot be disclosed here.) This surface treatment is considered to be a minor refurbishment as allowed under the X-34 contract.

Surface crack development and possible propagation into the interior were not modeled in this work. A charring material can develop surface wrinkles or cracks depending on the size of the heated article and the interplay of char shrinkage (minimal for SIRCA) and thermal expansion. These phenomena are acceptable only if they remain confined near the surface. Because it is not clear whether such cracks will develop in flight at lower heat flux and load, or whether the cracks will propagate owing to wing deflection, tile cracks will be monitored carefully during inspections of the flight vehicle.

A radiative equilibrium heating distribution was obtained from a GASP solution[8] for Mach 6.45 flow past the arc-jet model. The heating data were converted into convective heat transfer coefficient $C_T$ and recovery temperature $T_R$ distributions illustrated in Fig. 2. The transfer coefficient was scaled slightly to reproduce the stagnation point surface temperature expected during the tests. These two quantities are used in the surface boundary condition:

$$C_T(T_R - T_w) = \sigma\varepsilon\left(T_w^4 - T_\infty^4\right) + q_{\text{cond}} \qquad (1)$$

which allows consistent values of $q_{\text{cond}}$ and $T_w$ to be determined simultaneously as functions of time and surface location. The surface was assumed to radiate to an environment at $T_\infty = 70$°F, and the back surface of the model was assumed to be fully insulated.

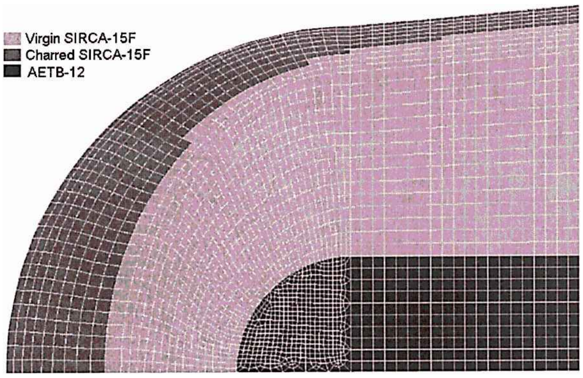

**Fig. 3 Arc-jet FE model.**

The initial temperature of the model was set at 70 or 90°F. This range of initial temperature was considered because in some cases the model did not completely cool to room temperature between cycles.

The thermal response on the plane of symmetry was simulated with a planar FE model of the upper half of the cross-section geometry. This planar approximation should capture the initial temperature rise measured by the thermocouples, but during cooldown the actual temperatures will decrease faster than the predictions owing to spanwise conduction effects. The FE grid is presented in Fig. 3. The tile is modeled as fully charred SIRCA at the surface and virgin SIRCA beneath that. The thermal properties of SilFrax foam were not available, so in the analysis the thermal properties of AETB-12 were used instead. The convective heating boundary condition, Eq. (1), was applied to the surface for 180 s (corresponding to the arc-jet test time) after which the left-hand side of the equation was set to zero, and the surface was allowed to cool by radiation for another 820 s.

The thickness of the char layer was determined by iteration using an expression that relates the residual level of silicone in an element to an integral of the temperature history for the element. SIRCA elements that were more than 50% charred (more than half the silicone pyrolyzed) were considered to be fully charred, and the material properties for these elements were set to the char values. All other SIRCA elements were assigned virgin properties. Three FE iterations were required to obtain a char distribution consistent with the temperature history for each element. This distribution, which approximates the char depth obtained after repeated heating cycles, is depicted in Fig. 3. The char depth varies from approximately 0.5 in. at the stagnation point to 0.2 in. on the shoulder under the assumed heat flux conditions. This predicted char-depth distribution was confirmed by inspection of the core samples taken from the 0-deg and 45-deg locations after 15 exposures. The char-depth history was not measured because doing so would destroy the model; furthermore, the char history is not particularly important to successful performance of the design. The thermal model indicates there should be little change in char depth after the second heating cycle. Material that reaches a temperature of about 800°F becomes fully charred on repeated exposure.

The temperature histories at the five reference points on the FE model are shown in Fig. 4. The stagnation point reaches a temperature of 2235°F, whereas the shoulder reaches 1430°F. The interior 0-deg point reaches a maximum temperature of 392°F at 735 s, whereas the interior 45-deg point reaches a maximum of 361°F at 770 s.

Figures 5 and 6 compare the arc-jet thermocouple data from the first 15 runs (excluding cycle 1) with the FE predictions at the 0- and 45-deg points, respectively. Individual runs are not identified in the figures because there is no discernable run-to-run trend in the data. Predictions were made for the nominal heating case with two initial conditions as well as 15% over and under heating. This range of heating is a typical variation that can be expected from run to run in arc-jet testing. The computed results show a reasonably good agreement with the data during the initial temperature rise but a higher maximum and slower temperature decrease at long time as expected owing to the limitations of the planar approximation.

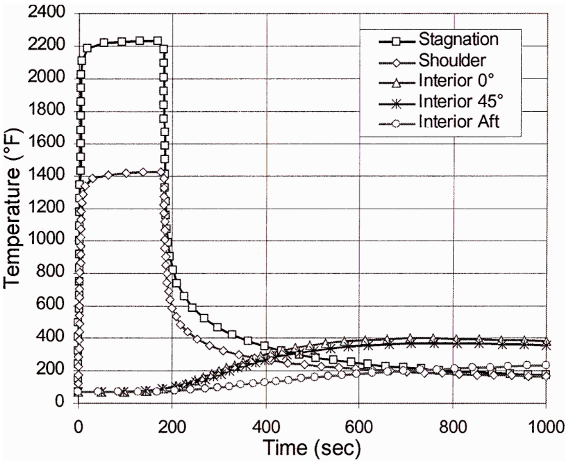

**Fig. 4 Temperature histories at reference points.**

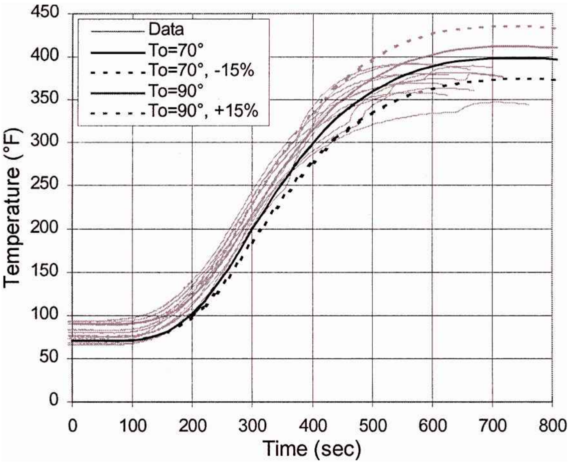

**Fig. 5 Temperature history at interior 0-deg point.**

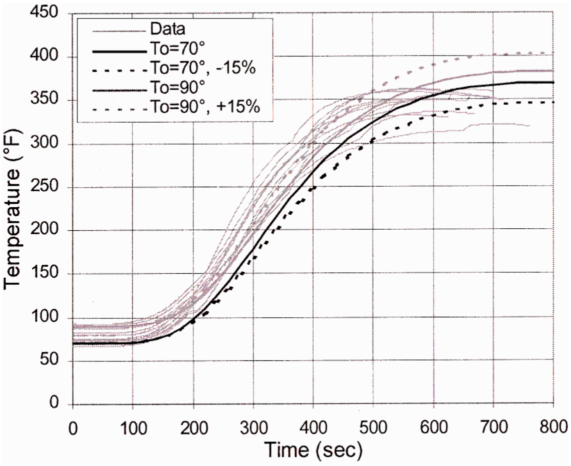

**Fig. 6 Temperature history at interior 45-deg point.**

### Mechanical Bending Tests

Room temperature three-point and cantilever-bending tests of bonded and unbonded SIRCA tiles were performed at NASA Ames Research Center. FE analyses of the tests used the orthotropic SIRCA mechanical properties listed in Table 3 with the transverse direction oriented in the direction of the applied load.

#### *Three-Point Bending Tests*

Two three-point bending experiments were conducted with SIRCA tiles bonded to aluminum plates. The geometry of the first experiment is presented in Fig. 7. A series of increasing static loads was applied to the test model that cracked at 360-lb load. The

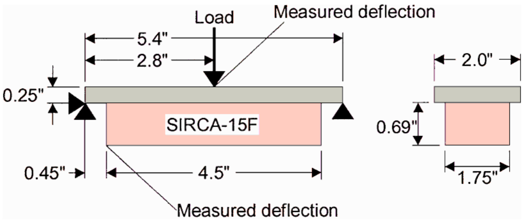

Fig. 7 Geometry of first three-point bonded tile-bending test.

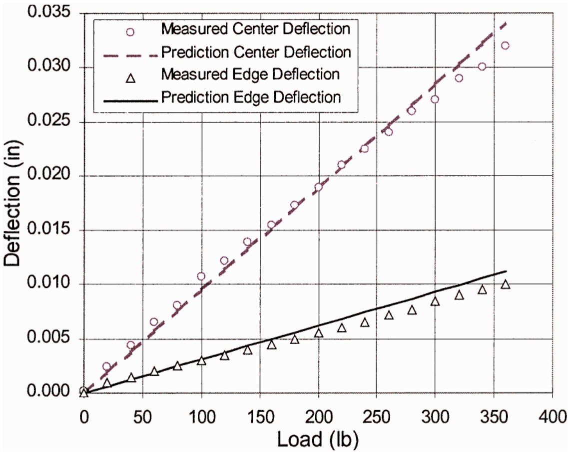

Fig. 8 Deflection results for first three-point bonded tile-bending test.

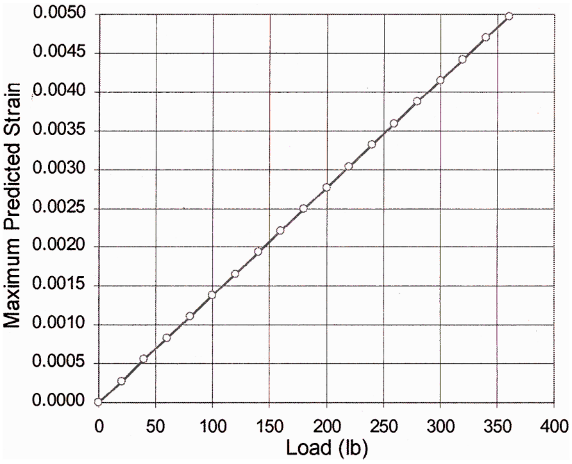

Fig. 9 Strain predictions for first three-point bonded tile-bending test.

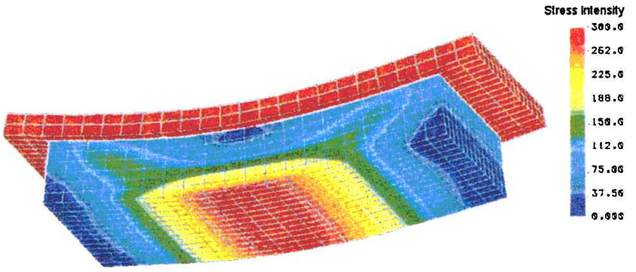

Fig. 10 Stress contours at 360-lb load with deflection magnified by a factor of 5.

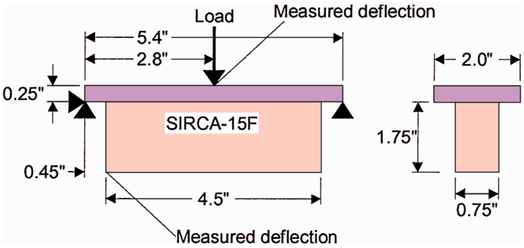

Fig. 11 Geometry of second three-point bonded tile-bending test.

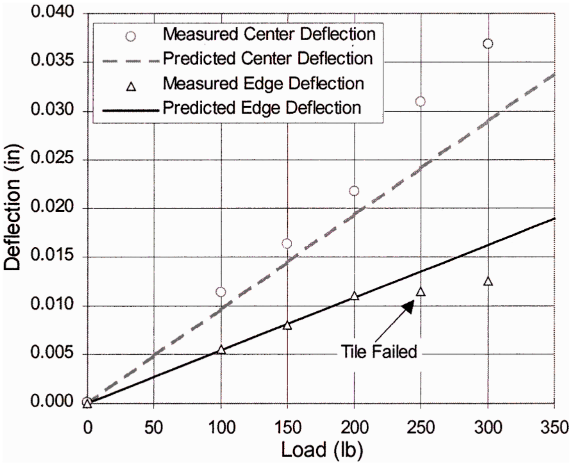

Fig. 12 Deflection results for second three-point bonded tile-bending test.

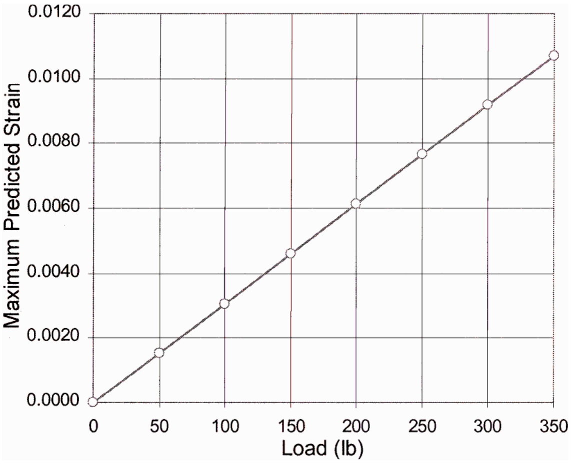

Fig. 13 Strain predictions for second three-point bonded tile-bending test.

measured and predicted deflections show excellent agreement in Fig. 8. The maximum predicted strain in the tile (Fig. 9) is about 0.5% at tile failure. Figure 10 illustrates contours of the stress distribution in the tile for the 360-lb load condition. The stress is maximum on the face opposite the applied load. The tile cracked at this location.

The geometry of the second experiment is presented in Fig. 11. A series of increasing static loads up to 300 lb was applied to the test model, but the tile cracked at 250-lb load, so the data above that point are of questionable value. The measured deflections and predicted deflection and strain are shown in Figs. 12 and 13. The deflection data at the edge of the tile show an excellent agreement with the predictions up to the point where the tile failed, but the data at the center location fall about above the predictions. However, the latter data appear to have a $y$-axis intercept of about 0.002 in. that suggests there was an offset error in the measurements. If 0.002 in. is subtracted from the center deflection data, then all data up to 200-lb load are within 5% of the predictions. The maximum predicted strain in the tile (Fig. 13) is somewhere near 0.7% at tile failure. Figure 14 illustrates contours of the stress distribution in the tile for the 250-lb load condition. The stress is maximum near the corner of the tile at the bond line. The tile cracked at this location.

### *Cantilever Bending Test*

A series of static loads up to 4.25 lb was applied to a bare SIRCA tile according to the cantilever geometry given in Fig. 15. For the finite element model calculations were performed using the nominal

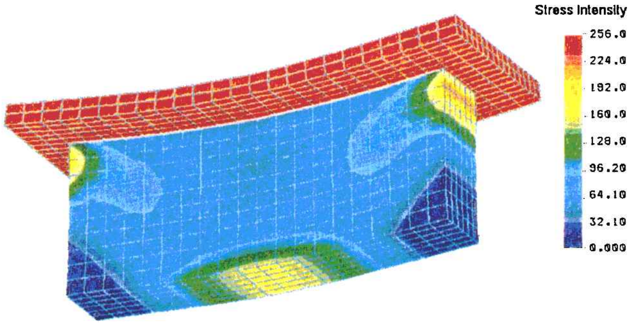

**Fig. 14 Stress contours at 250-lb load with deflection magnified by a factor of 10.**

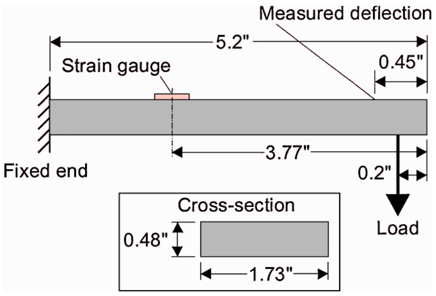

**Fig. 15 Geometry of cantilever-bending test.**

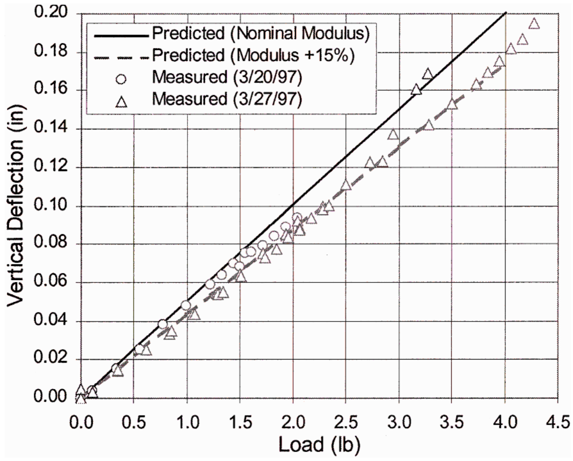

**Fig. 16 Deflection results for cantilever-bending test.**

tensile modulus given in Table 3 and also using a 15% larger modulus. The deflection and strain results at fixed measurement locations are shown in Figs. 16 and 17, respectively. Two experiments were performed on the same tile model at different times. The displacement data show a better agreement with the results using the higher modulus. The strain data from the earlier test (3/20/97) also show a good agreement with the results using the higher modulus, but the data from the later test are lower. One possible explanation for this discrepancy is the strain gauge may not have been located at exactly the same distance from the clamped end of the tile in the second test series. In any case the data suggest the sample tile was about 15% stronger than the nominal value listed in Table 3. Such a discrepancy is possible because the tabulated tile strength is a conservative value representing the lowest value expected from a number of samples. Figure 18 illustrates strain contours for a 4.0-lb load. As expected, peak compression and tension occur on the bottom and top, respectively, of the fixed end of the beam.

### *Summary*

The agreement between predictions and data for the bonded-tile three-point bending tests is excellent for both cases if one data set is corrected for an apparent offset error. A failure criterion of 0.5–0.7% strain is consistent with the loads required to crack SIRCA tiles in the tests. The agreement between the predictions and experimental results for the cantilever bending test is good if it is assumed the test sample had 15% above-nominal strength. However, the authors recommend continued usage of the more conservative (lower strength) data listed in Table 3 for all calculations.

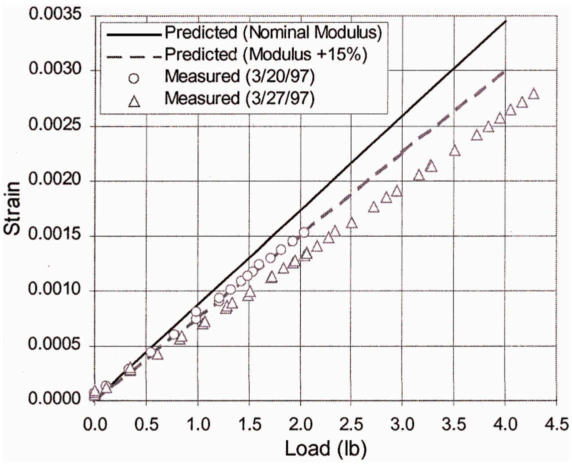

**Fig. 17 Strain results for cantilever-bending test.**

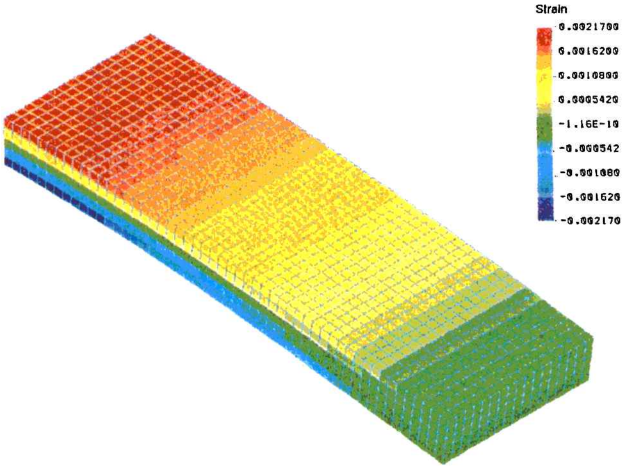

**Fig. 18 Strain contours for 4.0-lb load with deflection magnified by a factor of 2.**

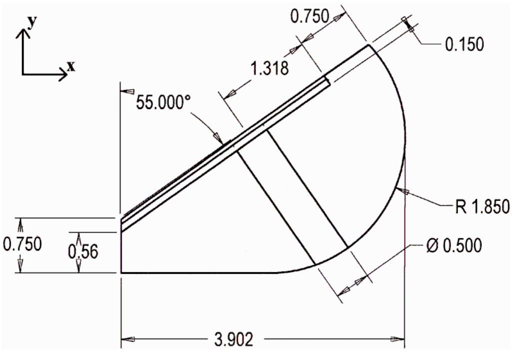

**Fig. 19 Cross section of wing leading-edge TPS components.**

The three-point bending test results support the assertion that the bond has higher strength than the tile. Therefore, if deflections become too high, the failure mode is tile fracture rather than bond failure. For directly bonded tiles this is a desirable fail-safe feature because tile fracture is not fatal, whereas bond failure may lead to loss of a tile.

## In-Flight Thermostructural Response

The X-34 wing leading-edge TPS design has an asymmetric canted cross section as shown in Figs. 19 and 20. The back face,

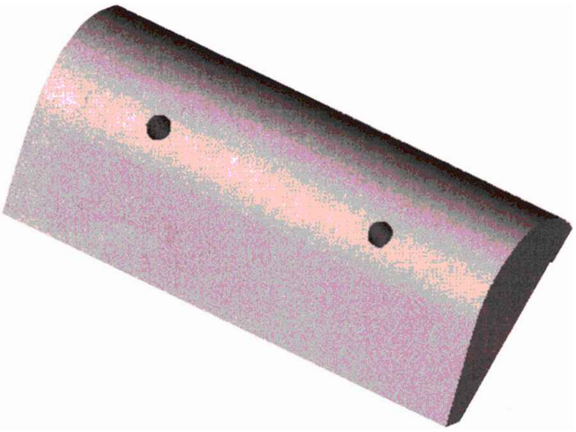

Fig. 20 Wing leading-edge solid model.

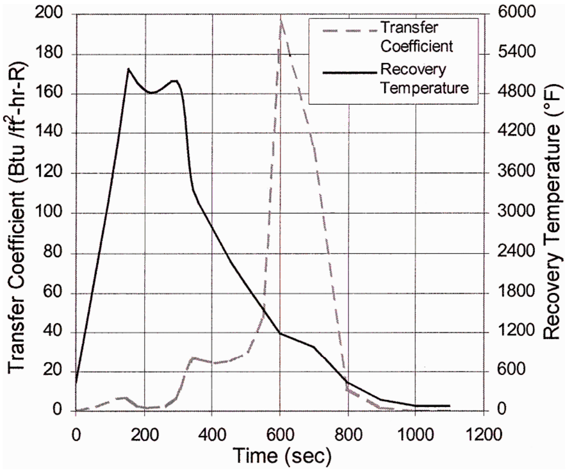

Fig. 21 Convective boundary conditions at one location on heated surface.

which is inclined at an angle 55 deg from vertical, is bonded to a 0.060-in.-thick graphite-epoxy (Gr/Ep) carrier plate using a 0.090-in. strain isolation pad (SIP). The bonding agent adds no additional thickness because it partially soaks into the SIP. The tile has a nominal 10-in. span in the direction normal to the cross section, and it contains two holes normal to the back face centered 5 in. apart. The carrier plate has smaller diameter holes that align with the holes in the tile. The tile is oriented with the transverse direction normal to the carrier plate.

The purpose of the holes is to allow the bonded assembly to be bolted to the wing leading-edge structure that contains nut inserts spaced every 5 in. along the wing span. After the carrier plate is bolted firmly to the structure, the holes are filled with tightly fitting bonded SIRCA plugs that provide good thermal and mechanical continuity across the plug-to-tile interface. If a tile must be removed, the holes are redrilled to provide access to the bolt heads.

Computational fluid dynamics predictions of wing heating for a conservative (severe) entry case were obtained by Palmer and Polsky[1] using the GASP code. The heating conditions vary along the span of the wing, and in most locations the heating is not severe enough to test any material thermal or mechanical limits. However, near the wing root bow-shock impingement causes a large localized increase in heating rate and load that potentially could be a problem. The focus of this section is the thermal and structural response of the wing leading-edge TPS assembly at this worst-case location. The heating data at the worst location were converted into a convective boundary conditions that vary with both time and location along the heated surface. For example, Fig. 21 shows $C_T$ and $T_R$ histories at a surface node near the peak heating location on the vehicle. Both parameters show two local maxima prior to 400 s that correspond to peak heating during ascent and descent.

A planar thermal analysis was performed to conservatively model the TPS response in the event the bow shock steadily impinges on one tile. The tile material was modeled as fully charred SIRCA at the surface and virgin material beneath that. The depth of the char layer was determined iteratively following the procedure described in the preceding section. The initial temperature was assumed to be −40°F, the surface was allowed to radiate to an environment at 70°F, and the back surface of the assembly was assumed to be fully insulated. The cold initial condition is a result of the long exposure of the vehicle on the L-1011 carrier aircraft prior to launch.

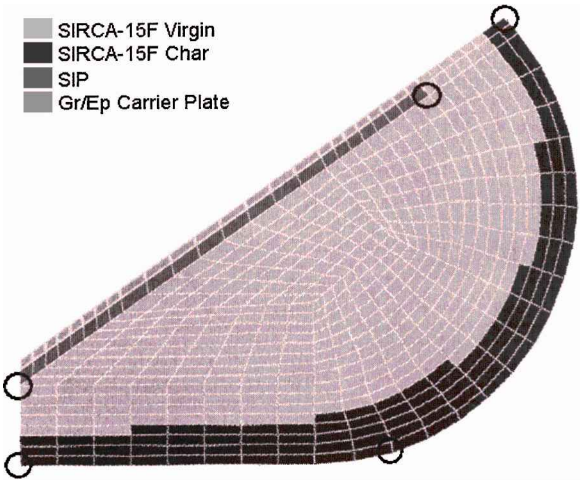

Fig. 22 FE model with char.

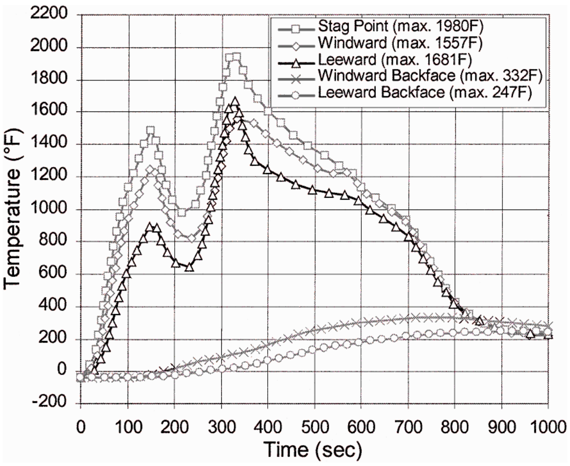

Fig. 23 Temperatures for charred model, $\varepsilon = 0.86$.

Because the arc-jet tests indicated that the char emissivity depends to some extent on the heating history and also can decrease gradually on repeated exposure, two constant surface emissivities of 0.86 and 0.65 were considered. Using methodology developed by Chen and Milos,[9] the boundary condition parameters $C_T$ and $T_R$ are relatively insensitive to changes in surface conditions; therefore, the same parameters can be used for both cases. However, the char depth was slightly different for the two cases. The FE model and char distribution for $\varepsilon = 0.86$ are shown in Fig. 22. The char thickness varies from 0.15 to 0.3 in. normal to the heated surface. The circles indicate locations at which temperature histories were tracked.

Figures 23 and 24 present the temperature histories at the five locations for the two cases. As indicated in the figure legends, the peak temperature is 124°F higher in the low emissivity case. The backface temperatures, however, differ only by a maximum of 25°F. The windward backface temperature maximum of 357°F for $\varepsilon = 0.65$ is only 7°F above the design goal. Therefore, a decrease in surface emissivity is not necessarily dangerous even at the bow-shock impingement location on the wing leading edge. Nevertheless, it may be prudent to apply an emissivity coating on tiles subject to bow- shock impingement if a color change from blackish to brownish-white is observed.

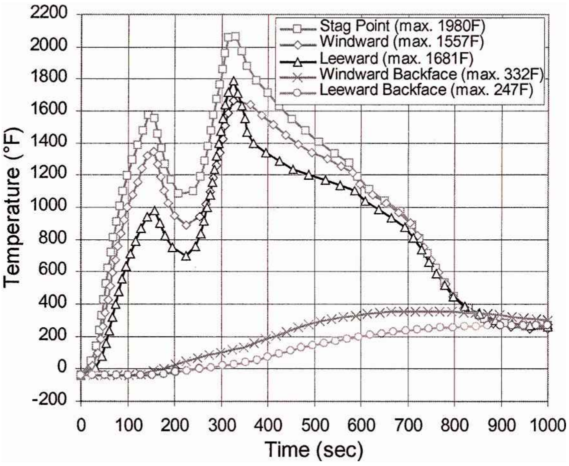

**Fig. 24 Temperatures for charred model, $\varepsilon = 0.65$.**

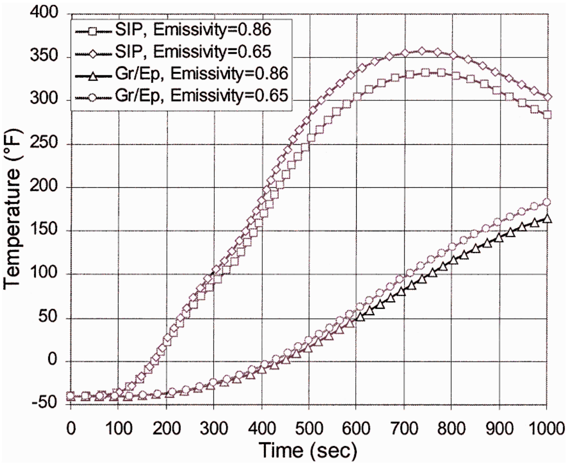

**Fig. 25 SIP and Gr/Ep carrier plate maximum temperatures.**

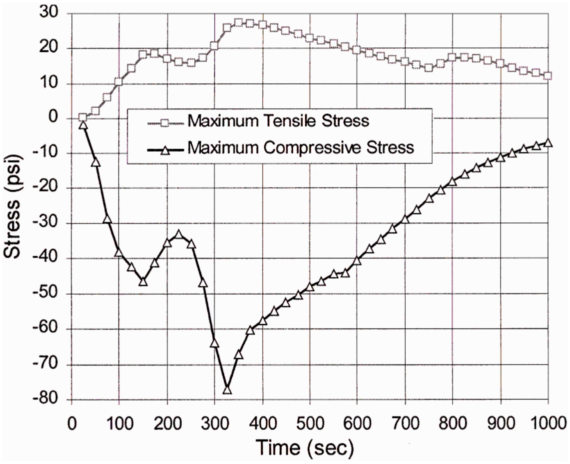

**Fig. 26 Maximum tensile and compressive stress histories.**

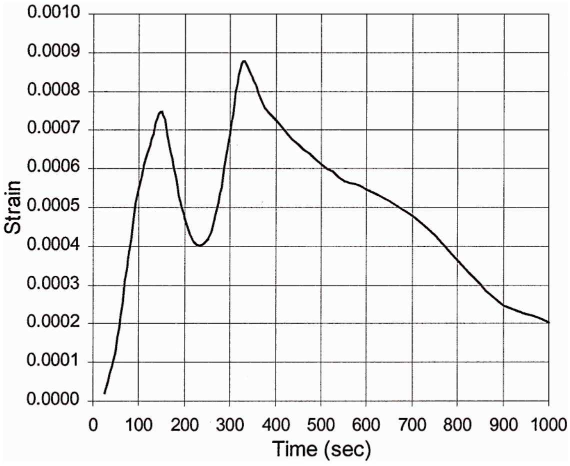

**Fig. 27 Maximum strain history.**

Figure 25 compares the maximum temperature history of the SIP and Gr/Ep carrier plate, regardless of location, for the two cases. The expanded vertical scale shows that the two cases differ by at most 25°F. Clearly the Gr/Ep temperature will not exceed the design goal of 300°F because the maximum temperature of the adjacent SIP is already decreasing below 300°F at 1000 s.

For the thermal stress analysis the planar model was extruded to form a 10-in.-long tile, and the temperature history was assumed to be invariant in the spanwise direction. The mechanical properties of the virgin and charred SIRCA were considered identical. For this analysis the bolt holes were not modeled because the bonded SIRCA plug is strain transmitting rather than strain isolating, and although there will be some thermal and mechanical property variations across the plug-to-tile interface, the actual variation cannot be prescribed with any certainty.

Figure 26 shows the maximum tensile and compressive stresses in the tile during the trajectory. These values represent the maxima throughout the entire tile rather than the stress at a fixed point. The maximum tensile and compressive stresses are 26 and 80 psi, respectively. These values are safely below the nominal transverse (weak direction) tensile strength of 108 psi and compressive strength of 140 psi. The peak compressive stress occurs at the same time as the peak temperature on the wing surface during entry. The peak tensile stress occurs about 25–40 s later. In general the stress extrema occur near the outer surface of the tile.

Figure 27 shows the maximum strain history throughout the tile. The predicted peak strain of 0.00092 is safely below the failure strain criteria of 0.005–0.007 established in the tile mechanical-bending tests. The two peaks in the strain history curve correspond to the two maxima in tile surface temperature.

These calculations included only the effect of differential thermal expansion; the effect of wing deflection will be considered in the next section. The results presented in this section indicate that thermal stress is not a problem for a 10-in. wing leading-edge tile in the flight environment considered in this study.

## Wing-Deflection Effects

Orbital Sciences Corporation conducted an extensive study of the structural performance of the X-34 vehicle. The study involved calculations of wing deflection for various load cases that included all aspects of flight from launch through landing. Examination of all cases reveals a maximum local strain of about 1.9% for the wing structure. This worst case is an upward (positive) bend that occurs at launch. The worst downward (negative) bend occurs on hard landing. The extreme local strain for downward deflection is about −0.8%.

These numbers are multiplied by a safety factor of 1.2 to obtain a limit value that represents the highest value which can be reasonably expected to occur in flight. Another multiplication by 1.5 produces an ultimate value that the vehicle is expected to survive, but with some repairable damage. Thus the overall ultimate deflection is 3.4%, but the ultimate downward deflection is −1.5%. The limit downward deflection is −1.0%.

The first issue to consider is the effect of wing deflection on a single-bolted TPS assembly. For upward deflection the wing structure pulls on the carrier plate via the bolt heads. For downward deflection the wing structure pushes on carrier plate that must deform similarly. The two cases are considered separately.

For the upward deflection case the three-dimensional FE model with tile, SIP, and carrier plate is shown in Fig. 28. Because the carrier plate is firmly bolted to the wing leading-edge structure, deflection loads were applied to the inner surface of the bolt holes on the carrier plate. One bolt hole was fixed, while the other had a differential deflection applied. Although the total strain occurs in

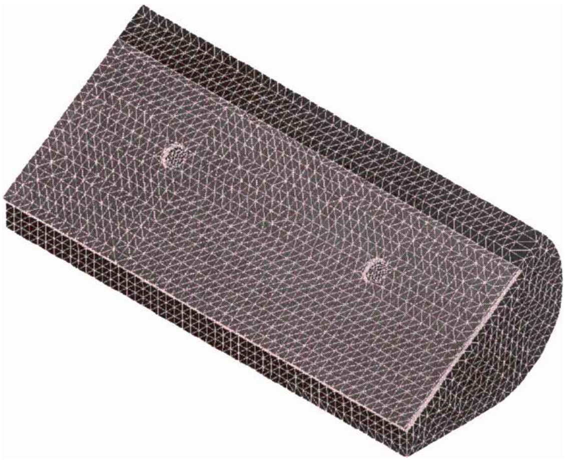

Fig. 28 Wing leading-edge FE model with holes.

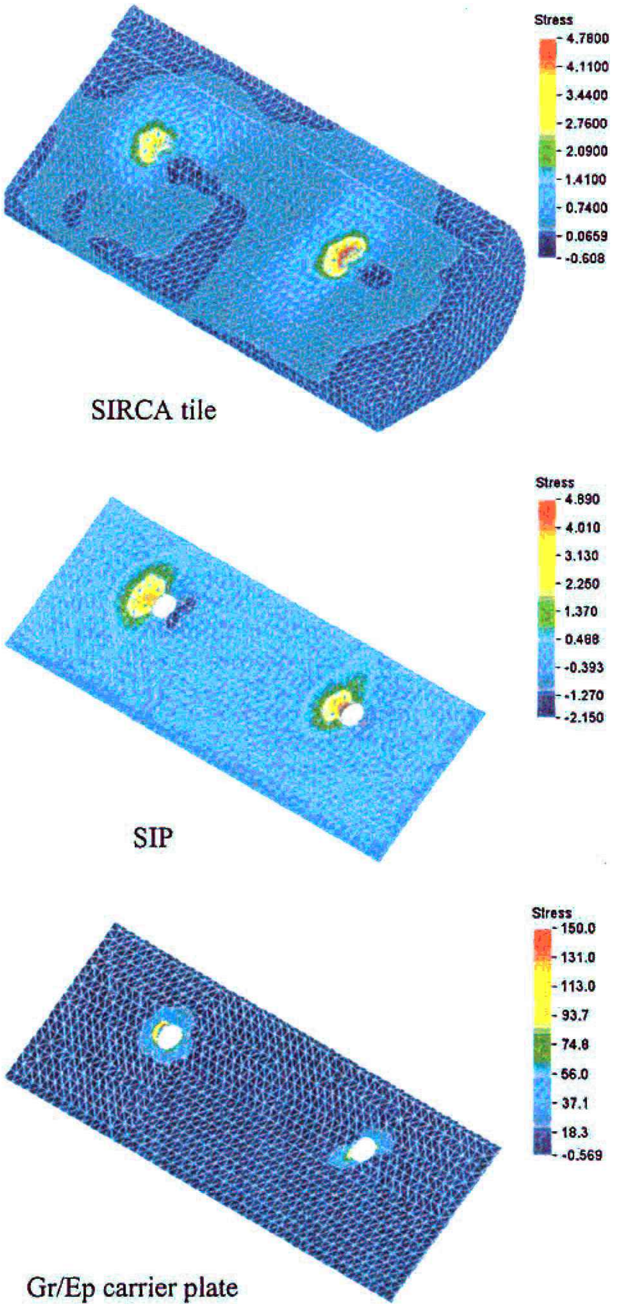

Fig. 29 Principal stress contours for individual materials for +3.4% deflection.

6 degrees of freedom, the majority of the strain (over 90%) is the result of bending in the vertical direction. Thus all of the deflection loading for this analysis was applied in the upward ($+y$) direction. The ultimate deflection of 3.4%, or 0.17 in. between bolt holes, was used.

Table 8 summarizes the maximum strain, tensile stress, and compressive stresses predicted in the model. The results show that the Gr/Ep plate experiences peak stress of 150 psi owing to its deflection. But the SIP absorbs almost most of the deflection, and the tile experiences almost negligible stress of less than 8 psi. Figure 29 illustrates stress contours in the Gr/Ep plate, SIP, and tile. Stresses are concentrated near the bolt connections but are well below the strength of the materials. The predicted peak strain in the tile of 0.0006 is an order of magnitude below the failure strain criteria established in the mechanical-bending tests.

The three-dimensional FE model for the downward deflection case is shown in Fig. 30. The model consisted of a 10-in.-long tile assembly attached to a 15-in.-long, 0.25-in.-thick aluminum plate. The bolt holes and bolt heads were not included; instead, the stiff plate was used to apply a prescribed downward deflection to the tile assembly. The plate was loaded by applying a given deflection to each end and fixing a point in the center of the plate.

Table 9 summarizes the maximum strain, tensile stress, and compressive stresses predicted in the model at −1.5% deflection. The maximum tensile and compressive stresses in the SIRCA tile are 61 and 79 psi, respectively. These values are safely below the nominal transverse (weak direction) tensile strength of 108 psi and compressive strength of 140 psi. The SIP and Gr/Ep stresses also are safely below the strength of these materials, and the predicted peak strain in the tile of 0.001 is safely below the failure strain criteria. Thus neither upward nor downward wing deflection appear to be a problem for this bolt attachment design with SIP. Figure 31 illustrates stress contours in the Gr/Ep plate, SIP, and tile. The stress maxima occur on the midplane of the geometry.

The second issue to consider is the effect of wing deflection on intertile gaps. Upward wing deflection is not a problem because such deflection is partially taken up by the SIP and although it opens up the gaps, no significant upward deflection occurs during high heating

Table 8 Results for 3.4% (upward) deflection

| Part | Maximum total strain | Maximum tensile stress, psi | Maximum compressive stress, psi |
|---|---|---|---|
| SIRCA tile | 0.0006 | 4.8 | 7.4 |
| SIP | 0.080 | 4.9 | 6.0 |
| Gr/Ep plate | 0.027 | 150.0 | 158.0 |

Table 9 Results for − 1.5% (downward) deflection

| Part | Maximum total strain | Maximum tensile stress, psi | Maximum compressive stress, psi |
|---|---|---|---|
| SIRCA tile | 0.001 | 61.4 | 78.7 |
| SIP | 0.157 | 7.1 | 12.9 |
| Gr/Ep plate | 0.0015 | 15.2 | 27.5 |

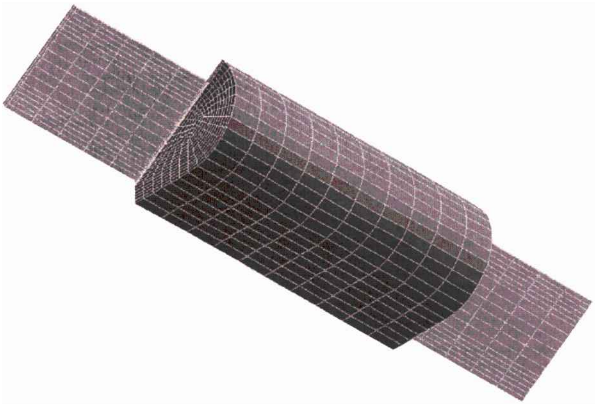

Fig. 30 Wing leading-edge FE model without holes.

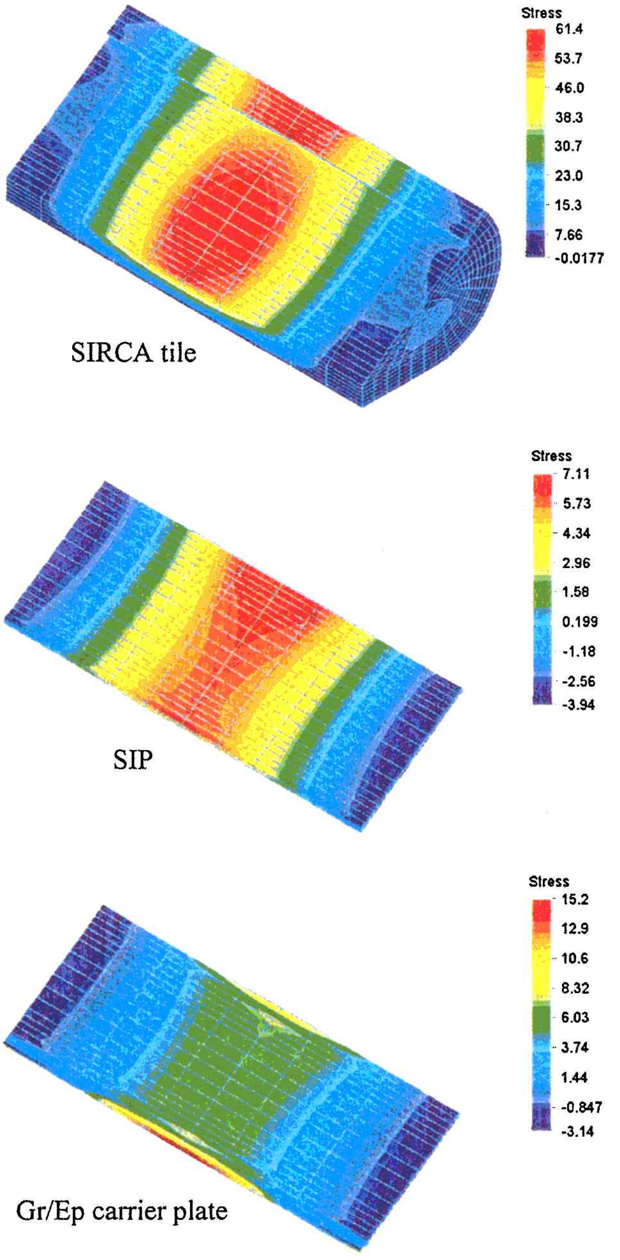
SIRCA tile

SIP

Gr/Ep carrier plate

**Fig. 31 Principal stress contours for individual materials for − 1.5% deflection.**

portions of the flight. Downward deflection is a serious concern because intertile gaps close and tiles may collide and thereby incur damage. The FE model consisted of two 10-in.-long tile assemblies mounted with a small intertile gap on a 15-in.-long, 0.25-in.-thick aluminum plate. The bolt holes were not included; instead, the stiff plate was used to apply a prescribed deflection to the tile assemblies. The assembly was loaded by applying a given deflection to each end of the aluminum plate and fixing a point in the center of the plate. Deflections of −0.25 to −1.75% were obtained by varying the load applied to the plate. Intertile gaps of 0.02 and 0.04 in. were considered. Two sets of calculations were performed.

The first set of calculations allowed the edges of the tiles to pass through each other as the structure deflection was increased. This procedure allowed the degree of interference to be determined. Figure 32 shows the tile interference as a function of wing deflection for both gap sizes. Negative values indicate that the edges of the tiles overlapped by the amount shown. The figure shows that for 0.02- and 0.04-in. gaps, deflections of about −0.5 and −1.0%, respectively, produce tile interference. At the ultimate negative strain of −1.5%, the tiles interfere by over 0.04 and 0.02 in. for the 0.02- and 0.04-in. gaps, respectively. But a gap of about just over 0.04 in. should prevent tile interference for the limit value of −1.0% deflection.

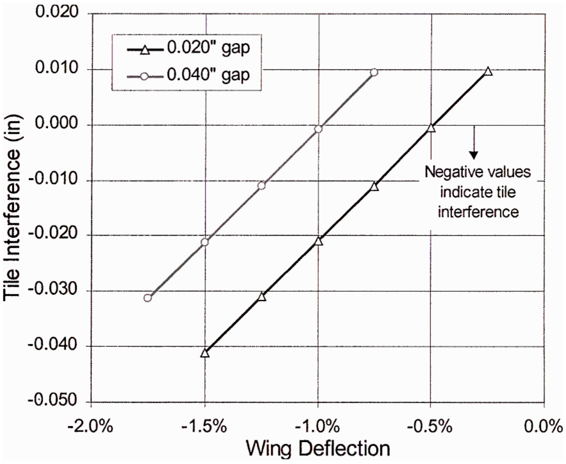

**Fig. 32 Maximum tile interference.**

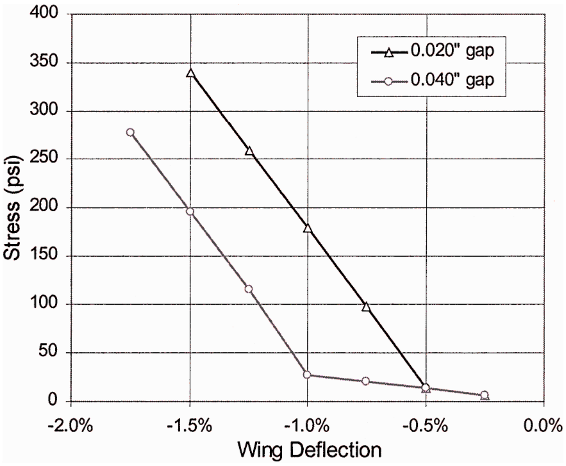

**Fig. 33 Maximum compressive stress in tile due to interference.**

**Fig. 34 Compressive stress contours at − 1.5% deflection.**

The second set of calculations included gap elements between the tiles that allow contact forces and stresses to be predicted. Figure 33 shows the maximum compressive stress at the contact point as a function of deflection for both cases. For the 0.02- and 0.04-in. gaps the stress exceeds the compressive strength of SIRCA at about −1.3 and −1.75% deflection, respectively. The stress concentration that occurs near the contact point is illustrated in Fig. 34, which shows a deflected shape and compressive stress contours for the case of −1.5% deflection and a 0.02-in. gap. Because contact only occurs at the nodes with gap elements, the stresses are concentrated at those points, and the magnitude may be exaggerated compared with an actual contact situation where the material can deform.

A third issue to be considered is heating that may result from flow into and through the intertile gaps during flight. This issue cannot be addressed readily by FE analysis; however, arc-jet testing and flowfield analyses will be conducted to investigate this phenomenon.

## Conclusions

Finite element thermal and stress analyses were presented for SIRCA tiles, assemblies, and arc-jet models relevant to the thermal protection system for the X-34 wing leading edge. The thermal and mechanical property models were shown to predict adequately the tile response in arc-jet and mechanical tests. A failure criterion for SIRCA tile of 0.5–0.7% local strain was established. The wing leading-edge tile design was demonstrated to have adequate thermal and structural margin for flight heating and mechanical loads. An intertile gap of about 0.04 in. is required to avoid collision of tiles for the limit-case downward deflection of the wing. Intertile gap heating and potential surface crack propagation issues still must be addressed.

## Acknowledgments

This work was partially supported by NASA Contract NAS2-14031 to ELORET. The GASP solution for the arc-jet flowfield was obtained by Y.-K. Chen from NASA Ames Research Center. Wing-deflection data were provided by Tom Dragone from Orbital Sciences Corporation. The SIRCA bend tests were performed by D. Tran and M. Smith at NASA Ames Research Center.

## References

[1] Palmer, G., and Polsky, S., "Heating Analysis of the Nosecap and Leading Edges of the X-34 Vehicle," *Journal of Spacecraft and Rockets*, Vol. 36, No. 2, 1999, pp. 199–205.

[2] Tran, H., Johnson, C., Rasky, D., Hui, F., and Hsu, M., "Silicone Impregnated Reusable Ceramic Ablators for Mars Follow-on Missions," AIAA Paper 96-1819, June 1996.

[3] Marschall, J., and Milos, F. S., "Gas Permeability of Rigid Fibrous Refractory Insulations," AIAA Paper 97-2479, June 1997.

[4] Milos, F. S., and Squire, T. H., "X-34 Tile Analysis Annual Report for FY97," X-34 Project Rept., NASA Ames Research Center, Oct. 1997.

[5] Lashkari, M., "COSMOS/M User's Guide, Volume 1," Structural Research and Analysis Corp., Santa Monica, CA, April 1992.

[6] Chen, Y.-K., and Milos, F. S., "Ablation and Thermal Response Program for Spacecraft Heatshield Analysis," AIAA Paper 98-0273, Jan. 1998.

[7] Squire, T. H., Milos, F. S., Hartlieb, G. C., and Rasky, D. J., "TPSX: Thermal Protection Systems Expert and Material Property Database," *ICCE/4 Fourth International Conference on Composites Engineering*, edited by D. Hui, ICCE, and College of Engineering, Univ. of New Orleans, New Orleans, LA, 1997, pp. 937, 938.

[8] McGrory, D. M., Stack, D. C., Applebaum, M. P., and Walters, R. W., *GASP Version 2.2 User's Manual*, Aerosoft, Inc., Blacksburg, VA, 1993.

[9] Chen, Y.-K., and Milos, F. S., "Solution Strategy for Thermal Response of Nonablating Thermal Protection Systems at Hypersonic Speeds," AIAA Paper 96-0615, Jan. 1996.

T. C. Lin
*Associate Editor*

**Color reproductions courtesy of NASA Ames Research Center**